



A novel approach to enhance the ionic conductivity of silver nanoparticles incorporated PVA:NaBr polymer electrolyte films via fast neutron irradiation

M.P. Shilpa^a, Vipin Cyriac^b, S.C. Gurumurthy^{a,*}, Ismayil^b, Sachin Shet^c, K.V. Subbaiah^c, M.S. Murari^d

^a Nano and Functional Materials Lab (NFML), Department of Physics, Manipal Institute of Technology, Manipal Academy of Higher Education, Manipal, 576104, Karnataka, India

^b Polymer Physics and Energy Storage Devices Lab, Department of Physics, Manipal Institute of Technology, Manipal Academy of Higher Education, Manipal, 576104, Karnataka, India

^c Manipal Centre for Natural Sciences, Manipal Academy of Higher Education, Manipal, 576104, Karnataka, India

^d DST PURSE Lab, Mangalore University, Mangalagangotri, Karnataka, India



ARTICLE INFO

Handling editor: Chris Chantler

Keywords:

Neutron irradiation
Solid polymer electrolytes
Ionic conductivity
AgNPs

ABSTRACT

This study investigates the unprecedented impact of fast neutron irradiation on the structural, electrical, and morphological properties of solid polymer electrolytes (SPEs). The SPE, a poly (vinylalcohol) (PVA)-sodium bromide (NaBr) based matrix with the incorporation of silver nanoparticles (AgNPs), was prepared via a solution casting method and subjected to various time intervals of fast neutron irradiation. X-ray diffraction (XRD) analysis revealed a distinct trend in the polymer electrolyte sample's amorphous phase, with decreased levels at lower neutron fluence and augmented levels at higher fluences. Fourier transform infrared (FTIR) spectroscopy highlighted plausible interactions leading to chain scission and cross-linking. Optical investigations below 300 nm exhibited increased absorbance and a shifted position of the surface plasmon resonance peak correlated with AgNPs. Validation of structural changes in the Ag-incorporated PVA-NaBr system was supported by reduced bandgap and elevation in Urbach energy, corroborating FTIR findings. Enhanced thermal stability was confirmed using thermogravimetric (TGA) analysis. Morphological modification upon irradiation were evident via Field emission scanning electron microscope (FESEM). Transport properties evaluated by Nyquist plot fitting showcased escalating room temperature conductivity with neutron fluence, and the highest conductivity obtained was 4.38×10^{-3} S/cm, an order higher than the pristine sample. Transference number measurements (TNM) indicated that the primary charge carriers are ions rather than electrons. This novel approach confirms that neutron irradiation can be used as a potential way to obtain highly conductive polymer electrolyte films.

1. Introduction

The search for advanced energy storage systems, characterized by high energy densities, power densities, long cyclability, flexibility, and environment-friendly nature, has surged these days due to high consumption of fossil fuels, rising crude oil prices, and population explosion leading to high energy demands (Torres et al., 2020). Presently, prevalent energy storage devices rely on liquid electrolytes formulated with carbonic esters and organic ethers due to their superior ionic conductivity and interfacial interactions. However, their susceptibility to serious safety issues like electrolyte leakage, decomposition, and

explosion presents significant challenges (Wang et al., 2020). Consequently, the exploitation of solid-state electrolytes such as ceramics, glasses, and polymers has gained traction, with solid polymer electrolytes holding particular promise (Long et al., 2016). Among them, solid polymer electrolyte is particularly interesting due to the enhanced safety, flexibility, and minimization of dendrite growth and reduction in the overall weight of the cell. Yet, their drawback lies in low ionic conductivity at room temperature (Arya and Sharma, 2017).

Several approaches have been extensively studied to enhance the polymer electrolytes' ionic conductivity, including polymer blending, adding plasticizers, copolymerization, cross-linking of polymers, the

* Corresponding author.

E-mail address: gurumurthy.sc@manipal.edu (S.C. Gurumurthy).

Table 1
Sample designation and neutron fluence.

Sample designation	Sample composition	Neutron irradiation time (days)	Neutron fluence rate (neutrons $\text{cm}^{-2}\text{s}^{-1}$)	Neutron fluence (neutrons cm^{-2})
S0	80 PVA: 20	0	–	–
S1	NaBr: AgNPs	19	5×10^3	8.21×10^9
S2	(from 6 mM	34		1.47×10^{10}
S3	AgNO ₃)	50		2.16×10^{10}
S4		96		4.15×10^{10}

addition of nanofillers, and irradiation (Ngai et al., 2016; Nanda et al., 2011; Althubiti et al., 2022). Among these, polymer irradiation is one of the effective approaches to obtain polymeric materials with unique properties for high performance applications. Irradiation using alpha particles, X-ray photons, electron beam, gamma-rays, proton, and swift ions facilitates tailored modifications in physical, chemical, thermal, structural, dielectric, and morphological properties (Althubiti et al., 2023a, b; Atta et al., 2022; Atta and Abdeltwab, 2021; Briskman, 2007; Croonenborghs et al., 2007; El-Malawy et al., 2023; Naikwadi et al., 2022; Raghu et al., 2016). The interaction of ionizing radiation with polymers generates highly reactive intermediate particles like ions, free radicals, and excited states, thereby inducing irreversible changes through bond breakage and formation (Williams, 1972). The degree of these changes depends on the target material, radiation energy, exposure time etc. (Abdul Rahaman et al., 2014). The intermediate particles cause chemical chain scission and/or crosslinking co-occurring in the polymer target. The crosslinking results in the formation of the new bonds and chain scission, leading to the polymers' fracture (Ferreño et al., 2018). The changes in the polymeric network depend on the competition between these two processes (Ghosal et al., 2013). The extent of chain scission/crosslink differs from one polymer to another depending upon the type of chemical bonds in the polymer matrix.

Notably, fast neutron irradiation presents an intriguing avenue. When fast neutrons are irradiated on organic materials, they primarily interact with the materials' protons, creating high-energy recoil protons due to inelastic collisions. Consequently, the chemical impact of fast neutrons is equivalent to that of high-energy protons. As the recoil protons and heavy ions in the compound play a vital role, rapid neutron irradiation of organic materials has a high linear energy transfer (LET). For instance, the LET value of 1 MeV fast neutrons in organics is over 100 times greater than that of the Co-60 gamma ray. Hence a significant difference in the effects of the neutron and gamma rays is expected (Tabata and Katsumura, 1985). Apart from this, neutron irradiation can cause irreversible changes to the polymeric structure, altering the properties.

Prior studies have reported the effect of fast neutron irradiation on the different polymers and polymer nanocomposites and the suitability of these materials for distinct applications. For instance, exposure of polyallelic diglycol carbonate (PADC) polymer to varied neutron fluence has resulted in fluence-dependent structural, optical, and chemical modifications (Kumar et al., 2011). A decrement in optical band gap and an increase in amorphousness at higher fluence indicated the formation of a defective polymer surface. Polymethyl methacrylate (PMMA) doped with Rhodamine B has shown enhanced linear and nonlinear optical characteristics under exposure to neutron radiation of low dosage (105 kGy) owing to the alteration of internal structure (Nafee and Hamdalla, 2019). The band gap, the intensity of the FTIR band, and the crystallinity were decreased for reactor-neutron irradiated polyethylene terephthalate (PET), with increased fluence representing the structural changes leading to total damage to the polymer network (Chikaoui et al., 2017).

Similarly, studies focusing on the neutron irradiation's influence on blended polymers such as polyvinyl alcohol/hydroxypropyl methylcellulose (Abdel-Zaher et al., 2016), polyvinyl alcohol/hydroxy propyl

cellulose (Abutalib and Guirguis, 2014), and polyvinylpyrrolidone/gelatine doped with dysprosium chloride (Basha and Basha, 2017) have been conducted. Furthermore, neutron irradiation on polymer nanocomposites like boron nanopowder, gadolinium, and boron carbide-loaded epoxy resin has significantly improved thermal stability and mechanical properties, suitable for neutron shielding applications (Abuali Galehdari and Kelkar, 2017). Epoxy-TiO₂ nanocomposite exhibited increased impedance upon irradiation, suggesting its applicability for electric power insulation in nuclear power plants.

Despite numerous studies on neutron irradiation effects on polymers, the impact of fast neutron irradiation on polymer electrolytes to improve their ionic conductivity remains unexplored. Hence, the present study aims to investigate the potential utilization of neutron irradiation on polymers to enhance the energy storage capability. PVA, a nontoxic, low-cost synthetic polymer known for its biocompatibility, biodegradability, flexibility, and high thermal and chemical stability offers excess -OH functionalities, acting as interaction sites for dissolved metal salts, making it an ideal polymer matrix in polymer electrolytes. Our previous work explored the suitability of silver nanoparticles to enhance the ionic conductivity of PVA-NaBr solid polymer electrolyte, revealing a one order enhancement in ionic conductivity (Cyriac et al., 2022a). The present work intends to analyze the impact of fast neutron irradiation on the ion conduction properties of solid polymer electrolytes in view of testing their suitability in energy storage devices.

2. Experimental methods

The preparation of silver nanoparticles through the chemical reduction method and incorporating them into PVA-NaBr polymer samples have been reported earlier in our previous work (Cyriac et al., 2022a), including the materials used for the preparation.

2.1. Neutron irradiation of the samples

In the present work, the optimum sample reported in our previous work (Cyriac et al., 2022a) (PNAg6, labeled as S0) was selected for neutron irradiation at various time intervals. Free-standing films of size 3 cm × 3 cm are placed at a distance of 10 cm from the 16 Ci Americium-Beryllium (AmBe) neutron source contained within a concrete bunker with a 40 × 40 × 70 cm³ irradiation channel. This source emits neutrons of a wide range of energies. Along with neutron, gamma radiation of energy 4.4 MeV is emitted. The neutron and gamma dose rate at the irradiation location is 12 and 0.3 mSv/hr, respectively. The flux from the source is about 5×10^3 neutrons $\text{cm}^{-2} \text{s}^{-1}$ at about 10 cm from the source. The samples were irradiated at different intervals, and the corresponding neutron fluence has been calculated and documented in Table 1.

2.2. Characterization techniques

The structural changes occurring due to neutron irradiation of the polymer samples were studied using Fourier transform infrared (FTIR) spectroscopy (Shimadzu IR Spirit instrument). The IR spectra were noted in the wavenumber range 400–4000 cm⁻¹ in the transmittance mode at a resolution of 4 cm⁻¹. The variations in the samples crystallinity were probed by X-ray diffraction (XRD) using a Rigaku Miniflex X-Ray diffractometer (5th Gen, 40 mA, 15 kV) using $K\alpha$ ($\lambda = 1.54 \times 10^{-10} \text{ m}$) radiation over the scattering angle $2\theta = 5$ to 50° with a step size of 1° min^{-1} . The optical bandgap and Urbach energy changes upon irradiation were investigated using UV-Visible spectroscopy using a Shimadzu 1900i UV-Vis double beam spectrophotometer in the wavelength range 190–1100 nm in absorbance mode. Room temperature (25 °C) impedance spectroscopy was performed using Agilent Precision impedance analyzer 4294 A from 100 Hz to 5 MHz. The samples were placed between two ion-blocking stainless steel

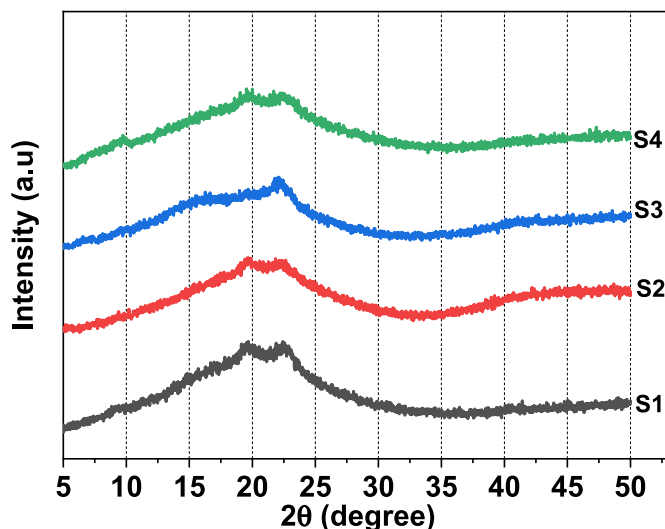


Fig. 1. XRD spectra of unirradiated and irradiated samples.

electrodes, and a constant ac signal of 50 mV was applied throughout the measurement. The inbuilt software in the instrument measures real (Z_r) and imaginary part (Z_i) of complex impedance, parallel capacitance (C_p) and tangent loss ($\tan \delta$) as a function of frequency. The data was later transformed into complex conductivity, dielectric and modulus formalism to study the ion dynamics in the irradiated samples. Variation of the thermal stability of the samples with neutron irradiation has been evaluated using Thermogravimetric analysis (TGA) with a Hitachi STA7200 TGA-DTA instrument by heating the sample under N_2 gas atmosphere (flow rate:20 mL min⁻¹) from RT-500 °C. The surface morphology of the samples has been studied using scanning electron microscopy (SEM) using Zeiss EVO 18 scanning electron microscope. Finally, the transference number measurement (TNM) has been performed using the Wagner polarization technique using Keithley source meter 2636 B. The samples are sandwiched between two stainless steel ion-blocking electrodes. A fixed dc voltage of 0.5 V is applied to this cell arrangement, and current is noted as a function of time.

3. Results and discussion

3.1. XRD studies

Most of the polymers are not entirely crystalline, with XRD spectra

displaying two components attributed to their crystalline and amorphous phases. The presence of an amorphous portion leads to the appearance of broad halos in the XRD pattern. To study the variation in the crystallinity with neutron irradiation, XRD analysis of neutron irradiated samples was performed. XRD pattern (Fig. 1) displays a broad halo from 5°-50° with distinct peaks. Sample S0 reveals distinct peaks of PVA at $2\theta = 19.5^\circ$ assigned to (101) and another shoulder peak at $2\theta = 22.9^\circ$ which is assigned to (200) crystal planes of PVA, indicating its semicrystalline nature as depicted in our previous study (Cyriac et al., 2022a; Zhu et al., 2013; Abd El-Kader et al., 2004). The semicrystalline nature is due to the inter/intra-molecular hydrogen bond in the PVA polymer (Saeed and Abdullah, 2020). With the increase in neutron irradiation fluence, the intensity of peak at $2\theta = 19.5^\circ$ is reduced, and is almost vanished for S3, indicating reduced polymer matrix crystallinity per the criteria proposed by Hodge et al. (1996). But with further increase in neutron fluence, the peak at $2\theta = 19.5^\circ$ reappears, indicating the increase in the crystallinity of the S4 sample. Further, the peak width is increased from S1 to S3 and is maximum for S3. The initial decrease in the crystallinity with an increase in fluence of the polymer samples, followed by the increase, indicates the fact that neutron irradiation is capable of causing structural variation/rearrangement of the polymeric network (Abutalib et al., 2015). Generally, the increase in the intensity of the XRD peak is attributed to the increase in the ordering due to degradation. The decrease in the intensity and broadening indicates the generation of disorderness due to the crosslinking, which destroys the crystallinity by inhibiting the recrystallization (Nouh et al., 2007; Nasef and Dahlán, 2003). To confirm the variation in the crystallinity, XRD deconvolution was attempted to deconvolute the XRD spectra into crystalline and amorphous peaks. We have reported the procedure of XRD deconvolution in our earlier studies (Cyriac et al., 2022b, 2022c).

Upon deconvolution, additional peaks could be revealed apart from those mentioned above (Fig. 2), which are assigned as crystalline/amorphous upon comparing it with the reported peaks of PVA (Abd El-Kader et al., 2004; Noor et al., 2013).

The degree of crystallinity χ (%) has been calculated from the area under the crystalline and amorphous peak using the following equation and is tabulated in Table 2.

$$\chi (\%) = \frac{\text{Area under all crystalline peaks}}{\text{Area under both crystalline and amorphous peaks}} \times 100\%$$

It is clear from Table 2 that crystallinity has reduced for lower fluence and has slightly increased for higher fluence.

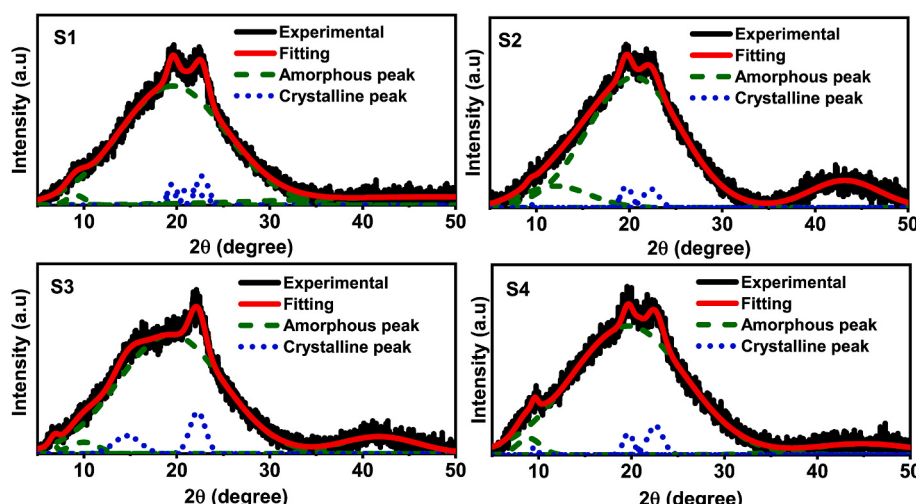


Fig. 2. Deconvoluted XRD spectra of unirradiated and irradiated samples.

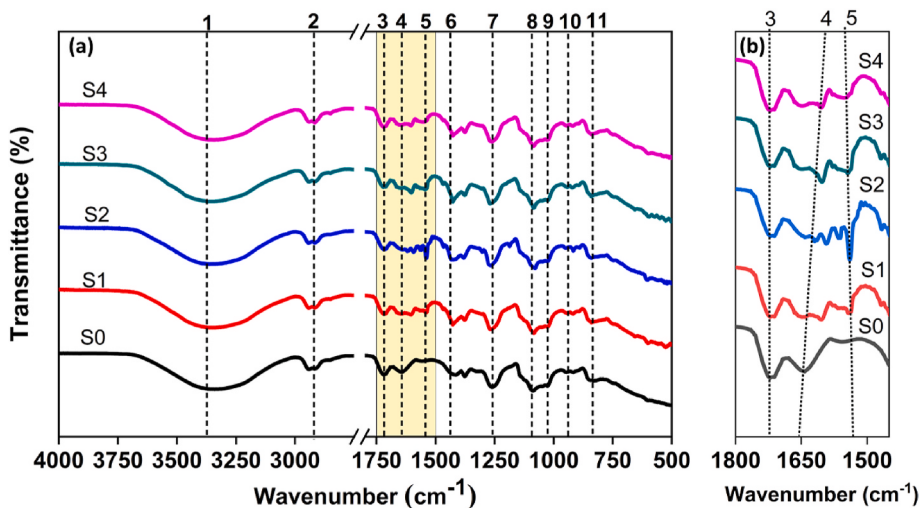


Fig. 3. (a) FTIR spectral assignments of unirradiated and neutron irradiated samples in 4000–500 cm⁻¹. (b) FTIR spectra in the region 1450 -1800 cm⁻¹ indicating variation in the intensity of C=O band (slanted line indicates the wavenumber shift; The spectra is stacked with equal offset values).

Table 2
Degree of crystallinity calculated from XRD spectra.

Sample	Area under all crystalline peak	Area under all amorphous peak	Degree of crystallinity χ (%)
S1	10623.26	2197.56	8.28
S2	630.423	10158.12	5.84
S3	448.53	10486.91	4.10
S4	417.93	9417.76	4.24

Table 3
IR band assignments for unirradiated and irradiated samples.

Wavenumber of major bands (cm ⁻¹)						Peak assignment in Fig. 3
S0	S1	S2	S3	S4	Peak assignment	
3341	3362	3364	3367	3344	-OH Stretching	1
2941	2941	2943	2941	2942	-CH asymmetric stretch	2
1721	1721	1720	1721	1721	C=O stretching of the acetyl group of PVA	3
1643	1643	1620	1603	1605	C=O/C=C stretching	4
1557	1542	1539	1544	1548	C=O stretch	5
1441	1427	1432	1427	1427	-CH ₂ scissoring	6
1376	1377	1361	1377	1376	-OH and CH bending	7
1261	1268	1261	1270	1260	-CH wagging	8
1088	1085	1079	1085	1088	C-O stretching	9
946	945	960	942	944	Skeletal vibration of PVA	10
830	840	840	840	840	Skeletal vibration of PVA	11

3.2. FTIR spectroscopic studies

Fig. 3 shows the IR spectra of unirradiated and neutron-irradiated samples in the 500- 4000 cm⁻¹ wavenumber range. Major absorption bands are identified and tabulated in Table 3 (Noor et al., 2013; Sagar et al., 2018; Guirguis and Moselhey, 2011; Htwe and Mariatti, 2020). The region below 1000 cm⁻¹ is the fingerprint region. The bands at 946 cm⁻¹ and 830 cm⁻¹ are attributed to the skeletal vibrations of PVA (Bhat et al., 2005). The region between 4000 cm⁻¹ to 1000 cm⁻¹ is the functional group region. The molecular interactions/structural

rearrangements can be found by observing the changes in the wavenumbers (greater than the resolution of the IR instrument, 4 cm⁻¹) and the change in the intensity of the bands.

3.2.1. Variation in the wavenumbers and intensity of the major bands:

- (i) The -OH stretching band, which appears at 3341 cm⁻¹ for the unirradiated sample, shifts to a higher wavenumber (3367 cm⁻¹) as we go from sample S0 to S3 and then later shifts to 3344 cm⁻¹ for S4. The increase in the wavenumber corresponding to -OH band, which might indicate the following possibility: On irradiation with neutrons, residual AgNO₃ further undergoes reduction by the generated hydrogen free radicals giving rise to more AgNPs (Basha and Basha, 2017). The AgNPs can form a bond with the -OH group of the PVA-NaBr matrix due to the oxidizing nature of OH free radical, thereby disrupting the inter/intra molecular hydrogen bonding as indicated in our previous studies (Cyriac et al., 2022a; Chahal et al., 2012; Naghavi et al., 2010). This is in correlation with a decrement in the peak intensity of (101) XRD peak at $2\theta = 19^{\circ}$ for S0-S3 (see section 3.1). However, with higher fluences, owing to the agglomeration of AgNPs, the possibility might be comparatively less, resulting in the shifting of the band to the lower wavenumber. These observations are in correlation with UV studies.
- (ii) The wavenumber corresponding to C=O stretching, which is assigned at 1643 and 1557 cm⁻¹, shifts to the lower wavenumber side as we move from S0 to S3 and then slightly shifts to the higher wavenumber side for S4. Also, we see the intensity of the C=O band at 1500-1750 cm⁻¹ increases as we move from S0 to S3 and then reduces for S4 (refer to Fig. 3(b)). The increase in the intensity of the carbonyl band may be due to the esterification of the hydroxyl group, which resulted in the stretching vibration of the C=O of the ester forming interpenetrating crosslink structure (Sinha and Rout, 2008; Rivaton et al., 2010). The drop in carbonyl group transmission intensities for the S4 sample is related to the cleavage of the carbonate linkage and the detachment of the hydrogen bonds from the polymer's backbone (Basha and Basha, 2017; Kumar et al., 2012).

This can be understood in the following way: In the presence of oxygen, the mechanism of radiolysis of PVA ought to be that oxygen reacts with the polymer radicals produced during irradiation to form polymeric peroxide (ROO[·]) radicals. These ROO[·] radical removes hydrogen atom from the polymer chain and converts it to hydroperoxide. This

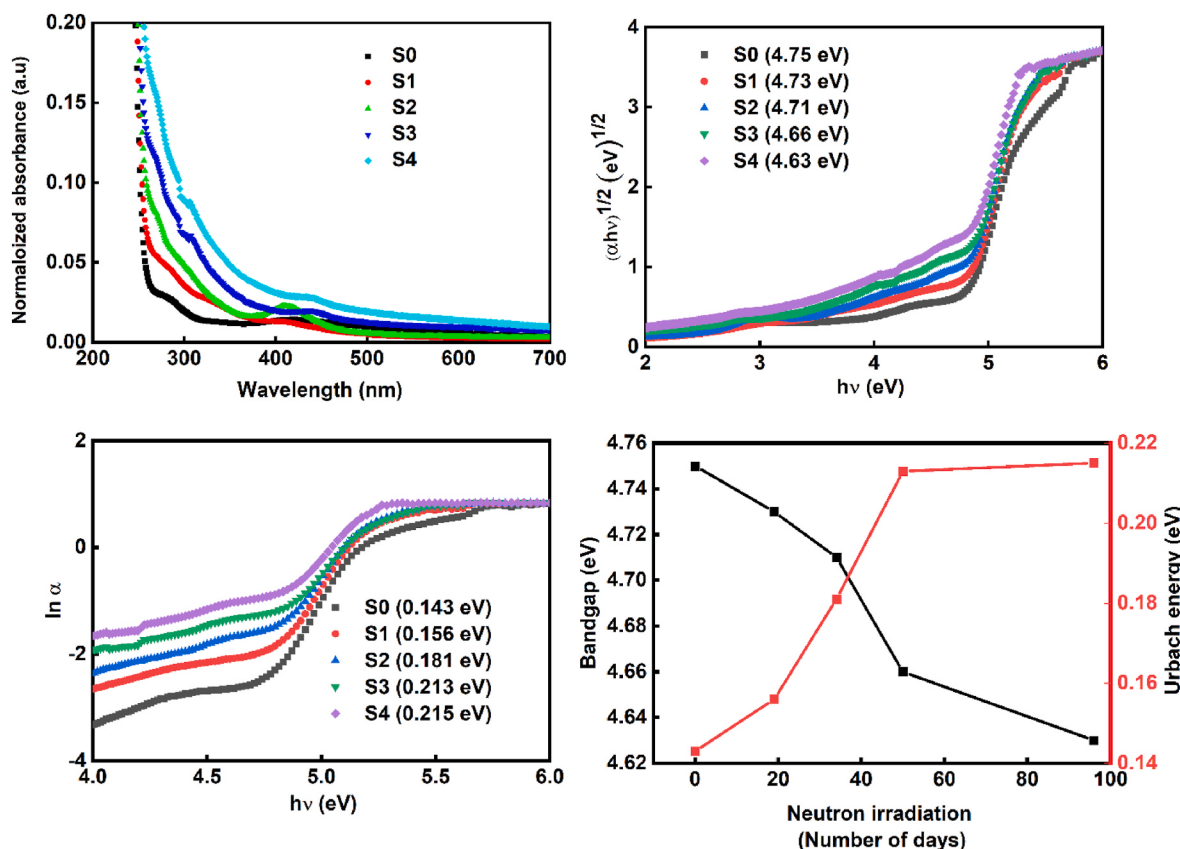


Fig. 4. (a) Absorbance plot. (b) Tauc plot for direct transition. (c) Plot of $\ln \alpha$ versus $h\nu$ (d) Plot showing the variation of bandgap and Urbach energy for unirradiated and irradiated samples.

Table 4

Absorption edge, position of SPR peak of Ag, bandgap, and Urbach energy for unirradiated and irradiated samples.

Sample	Absorption edge (nm)	Position of SPR peak (nm)	Bandgap (eV)	Urbach energy (eV)
S0	256	417	4.75	0.143
S1	259	411	4.73	0.156
S2	261	411	4.71	0.181
S3	263	435	4.66	0.213
S4	271	438	4.63	0.215

removal of hydrogen from the polymer chain could generate carbonyl compounds and hydroperoxides simultaneously (El-Sawy et al., 2010). The hydroperoxide further decomposes, causing the main chain of PVA to rupture primarily affecting the tertiary carbon atoms. Alternatively, the ROO^\cdot radical can crosslink at the alpha carbon to form interpenetrating network (Gongxu et al., 1993; Philipp and Hsu, 1979). Hence the radicals formed in these reactions lead to polymer cross-linking and chain scission (Abd El-Kader et al., 1999). Consequently, at lower fluence, the crosslinking of PVA dominates, whereas chain scission dominates at higher fluence, which agrees with UV-Visible spectra and XRD outcomes. The higher fluences, the chain scission occurs at the carbonate linkage leading to the decrement in C=O IR band intensity (Prasher and Kumar, 2019). Additionally, its important to note that trapped water molecules in the PVA-NaBr matrix, when exposed to neutron irradiation, might also lead to the formation of hydroxyl radicals (OH^\cdot) and hydrogen radical (H^\cdot), contributing to PVA's radiolysis.

3.3. UV-Visible studies

Insight into the impact of neutron irradiation on optical properties

and bandgap with respect to elevation in fluence can be acquired by UV-Visible studies. Fig. 4(a) shows the absorption spectra of pristine and neutron-irradiated polymer films. The absorption edge of the S0 appears at 263 nm. In our previous work (Cyriac et al., 2022a), the pure PVA- NaBr system depicted an absorption edge at 244 nm. The red shift of the absorption edge from 256 to 271 nm after incorporating AgNPs clearly shows the decrease in bandgap (Fig. 4(d)). This can be attributed to the formation of localized energy states, which may act as trapping and recombination centres (Nouh et al., 2007). In addition, the absorbance of S0 is considerably minimum compared to S1, S2, S3, and S4. The rise in absorbance below 300 nm with an increase in fluence is noticeable in all the samples. This might be attributed to the increased $\pi \rightarrow \pi^*$ transitions originating from additional unsaturated bonds like C=O, generated by the esterification of the hydroxyl group (Kumar et al., 2011; Nafee and Hamdalla, 2019; Eisa et al., 2011). These results are in congruence with FTIR results.

The appearance of a peak around 409–434 nm is due to the surface plasmon resonance effect (SPR) effect of AgNPs. At lower fluence, the enhancement in the SPR peak with a slight blue shift and narrowing of the latter peak can be ascribed to the complete reduction of unreacted $AgNO_3$ due to the direct redox reaction between PVA and residual Ag^+ ions, forming more Ag nanoparticles of smaller size in PVA-NaBr matrix. However, it is evident from Fig. 4(a) that at higher fluence, SPR peak with diminished intensity and significant bathochromic shift is observed. The mechanism behind shifting and change in intensity of the SPR peak can be attributed to the structural modifications of the polymeric chain. The crosslinked structure can create a three-dimensional network, which can significantly increase the molecular mass, and this three-dimensional polymer network with increased density around the nanoparticle can prevent aggregation, thus yielding smaller particles in the PVA-NaBr matrix. At higher fluence, the possibility of chain scission

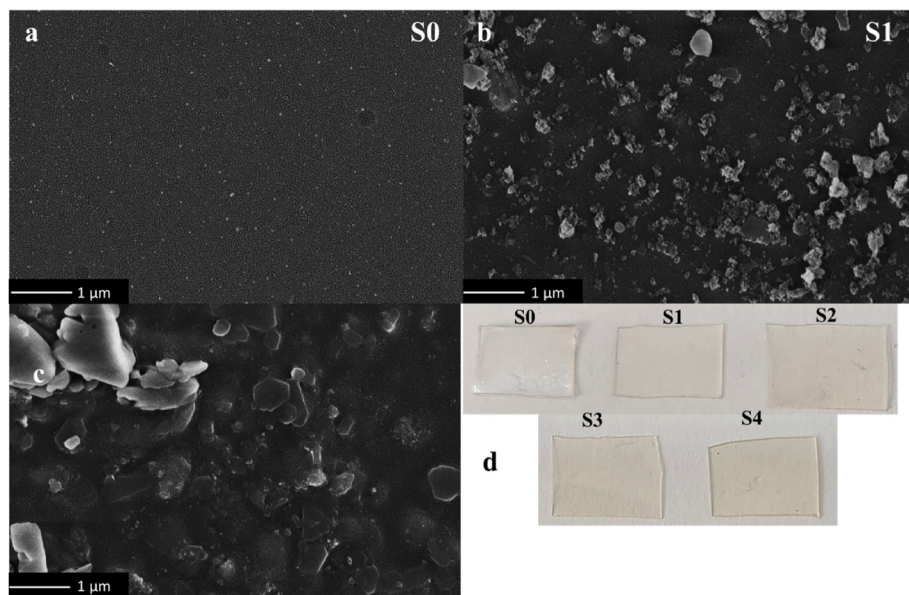


Fig. 5. SEM micrographs of unirradiated (S0) (a) and irradiated samples S1 and S4 (b&c). (d) Digital images of unirradiated and irradiated films.

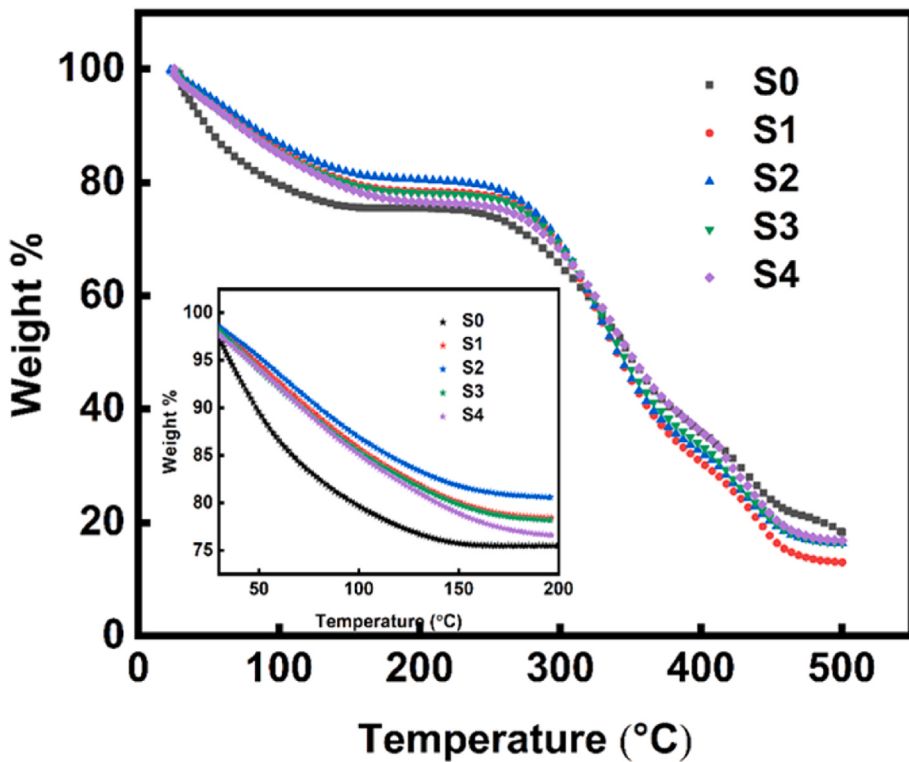


Fig. 6. TGA curves of unirradiated and irradiated samples.

is high. As the polymer chain gains mobility and releases stress, it can make AgNPs move inside the matrix, thus causing agglomeration. Z. I. Ali et al. obtained similar results with increased gamma irradiation on Ag/PVA nanocomposite films (Eisa et al., 2011; Ali et al., 2014)

The optical energy bandgap (E_g) can be obtained by the following equation (Nafee and Hamdalla, 2019)

$$\alpha h\nu = \beta (h\nu - E_g)^n$$

where, α , β , and $h\nu$ are absorption coefficient, structure-dependent factor, and photon energy, respectively, and n is the index that takes

the value according to the transition mode. The direct bandgap can be calculated by plotting $(\alpha h\nu)^{0.5}$ as a function of photon energy, $h\nu$. Extrapolating the linear portion of the plot to the x-axis allows determination of the x-intercept of the curve yielding the value E_g as shown in Fig. 4(b). It has been observed that the bandgap decreases from 4.75 to 4.63 eV with increased irradiation time, indicating the decrease in the films resistivity. The decrement in bandgap, corresponding to rise in fluence, may be attributed to the formation of localized energy states resulting from structural changes in the polymer (Nouh et al., 2007)

The π -electron carrying free radicals can cause structural disorders in

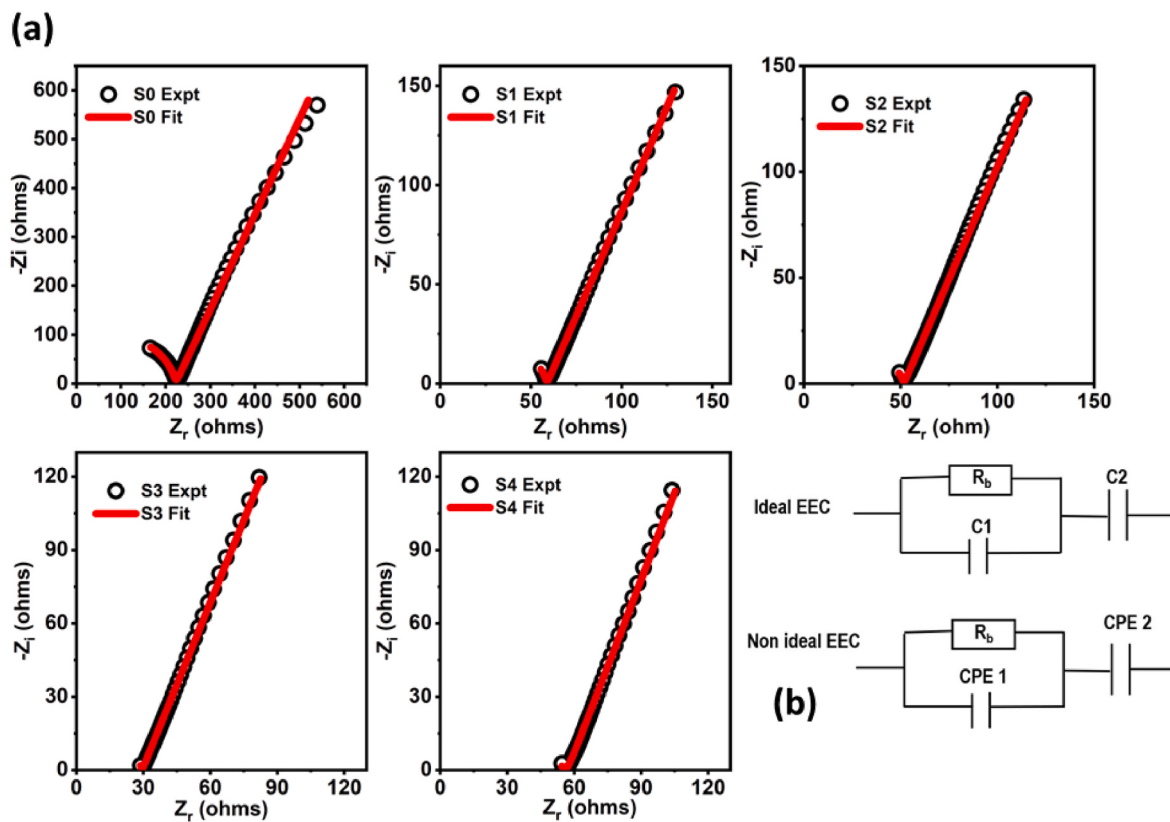


Fig. 7. (a) Nyquist plot of unirradiated and irradiated samples (b) with electrical equivalent circuit used for fitting.

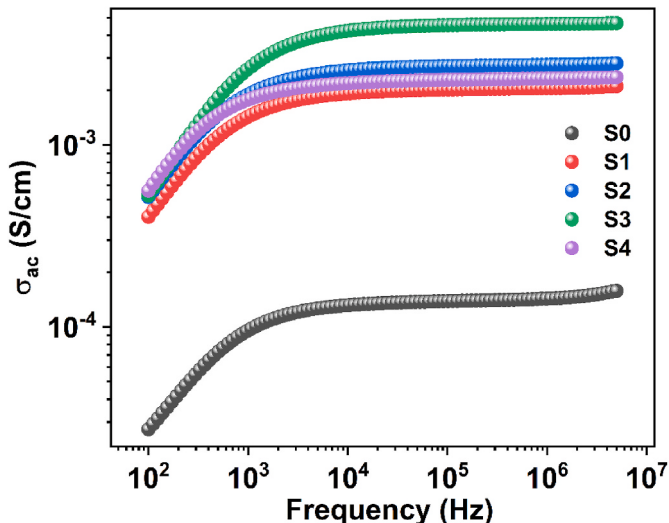


Fig. 8. AC conductivity spectra of the unirradiated and irradiated samples.

amorphous or semicrystalline materials, which can induce a dense, localized state between valence and conduction bands, known as Urbach energy or Urbach tail. Urbach energy can be used to characterize the degree of disorder or structural imperfections in the material. The Urbach energy can be defined by the following relation (Bafandeh et al., 2016)

$$\alpha h\nu = \alpha_0 \exp \frac{h\nu}{E_U}$$

where, α_0 and E_U are constant and Urbach energy, respectively. E_U is determined by the inverse of the slope of the plot, $\ln \alpha$ Vs $h\nu$. As evident

Table 5

Variation of bulk resistance (by intercept and EEC method), bulk conductivity, and ac conductivity for irradiated and unirradiated samples.

Sample	Bulk resistance R_b by intercept method (Ω)	Bulk resistance R_b by EEC method (Ω)	Bulk conductivity σ (S/cm) by Nyquist plot	DC conductivity σ (S/cm) by AC conductivity
S0	223.53	222.14	1.40×10^{-4}	1.20×10^{-4}
S1	58.61	58.85	2.02×10^{-3}	1.85×10^{-3}
S2	52.02	51.71	2.71×10^{-3}	2.14×10^{-3}
S3	29.48	29.50	4.58×10^{-3}	4.23×10^{-3}
S4	56.39	57.55	2.23×10^{-3}	2.55×10^{-3}

from Fig. 4(c) and (d), Urbach energy rises with the increase in fluence, clearly indicating the formation of increased defects with respect to the increased exposure to fast neutrons, thus enhancing the amorphousness of the samples (Nouh et al., 2007; Bafandeh et al., 2016). Further, XRD analysis obeys a similar trend.

Interestingly, the bandgap and Urbach energy variation is significant from a fluence of 8.21×10^9 to 2.16×10^{10} neutrons cm^{-2} . However, despite a significant increase in fluence, change in bandgap and Urbach energies are minimal beyond this fluence range.

The absorption edge, position of SPR peak of Ag, bandgap, and Urbach energy are summarized in Table 4.

3.4. Scanning electron microscopy

Fig. 5 reveals the morphology of the samples before and after irradiation. S0 portrays a smooth surface with uniformly distributed AgNPs. However, post-irradiated samples show morphological changes, as depicted in Fig. 5b and c. S1 and S4 depict a rough and coarse surface with irregularities (Sinha and Rout, 2008). The roughening of the surface after irradiation is primarily due to the formation of new bonds and

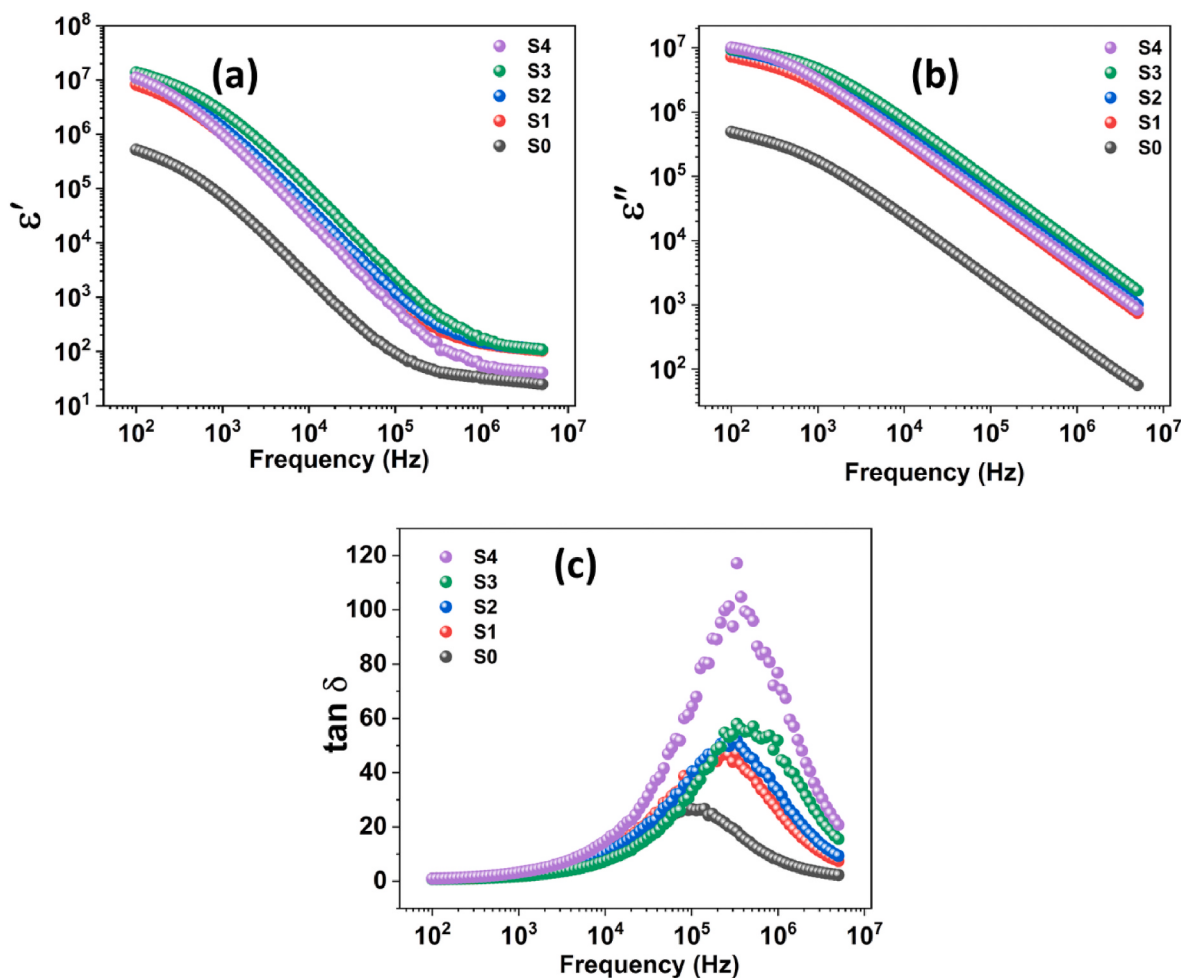


Fig. 9. Plot of (a) real part of permittivity, (b) imaginary part of permittivity, (c) tangent loss of unirradiated and irradiated samples.

Table 6
Variation of the parameters k_2^{-1} , D, μ and n for irradiated samples.

Sample	$k_2^{-1} \times 10^{-5}$ (F)	ϵ' at 100 Hz	D ($\text{cm}^2 \text{s}^{-1}$)	$\mu (\text{cm}^2 \text{V}^{-1} \text{s}^{-2})$	$n \times 10^{22}$ (cm^{-3})	σ (Scm^{-1})
S1	5.98	8.20×10^6	2.01×10^{-9}	7.84×10^{-9}	1.55×10^{23}	2.03×10^{-3}
S2	6.54	1.10×10^7	1.57×10^{-9}	6.13×10^{-9}	2.37×10^{23}	2.71×10^{-3}
S3	6.79	1.38×10^7	2.57×10^{-9}	1.00×10^{-9}	2.35×10^{23}	4.58×10^{-3}
S4	6.55	1.11×10^7	3.97×10^{-8}	1.55×10^{-6}	9.03×10^{22}	2.24×10^{-3}

the scission of existing bonds, indicating the initiation of polymer deterioration (El-Zahhar et al., 2020). The fast neutron-induced free radicals can cause various irradiation effects responsible for the evolution of the gases from the surface and oxidative embrittlement (Mathakaria et al., 2014). The evolution of gases or surface particle erosion occurs unevenly throughout the surface, resulting in defects on the surface of S1 and S4. This findings align with the FTIR results, clearly illustrating crosslinking and chain scission phenomena. Notably, the degree of smoothness decreases as the neutron fluence increases.

3.5. Thermogravimetric analysis

Fig. 6 depicts the thermogram for unirradiated and neutron-irradiated samples, measured from room temperature to 500 °C. The

thermogram confirms three distinct degradation stages for both sets of samples. The initial weight loss observed between 27 °C and 100 °C results from the removal of surface-absorbed moisture. Subsequently, between 100 °C and 300 °C, there is a 20% weight loss due to the detachment of water molecules linked strongly to hydroxyl groups (Cyriac et al., 2022a). The major weight loss (60%) beyond 300 °C up to 500 °C owes to the decomposition and carbonization of the PVA (Gomaa et al., 2018). A considerable increment in decomposition temperature (T_d) was observed after neutron irradiation, clearly indicating certain structural changes. Fig. 6 shows that the thermal stability after irradiation increases from S0 to S2, beyond which reduction in thermal stability is observed. Hence it can be again verified that at lower fluence, cross-linking of polymers is prominent, whereas scission of main chain dominates at higher fluence. Further, amount of weight loss due to removal of water (27 °C–100 °C) has been decreased after neutron irradiation (Inset of Fig. 6). This can be attributed to the radiolysis of water to free radicals, which aids the crosslinking of polymer chains.

3.6. Room temperature impedance spectroscopy

Understanding the ionic conductivity post-neutron irradiation involves analyzing the Nyquist plot (plot of Z_r versus $-Z_i$). The plot features a depressed semi-circular arc at high frequency and a slanted spike at low frequency (Fig. 7(a)). Interpreting the Nyquist plot involves considering the physical processes occurring during the ac impedance measurement. Hence, the low-frequency spike represents the capacitance of the double layer at the electrode-electrolyte interface due to the

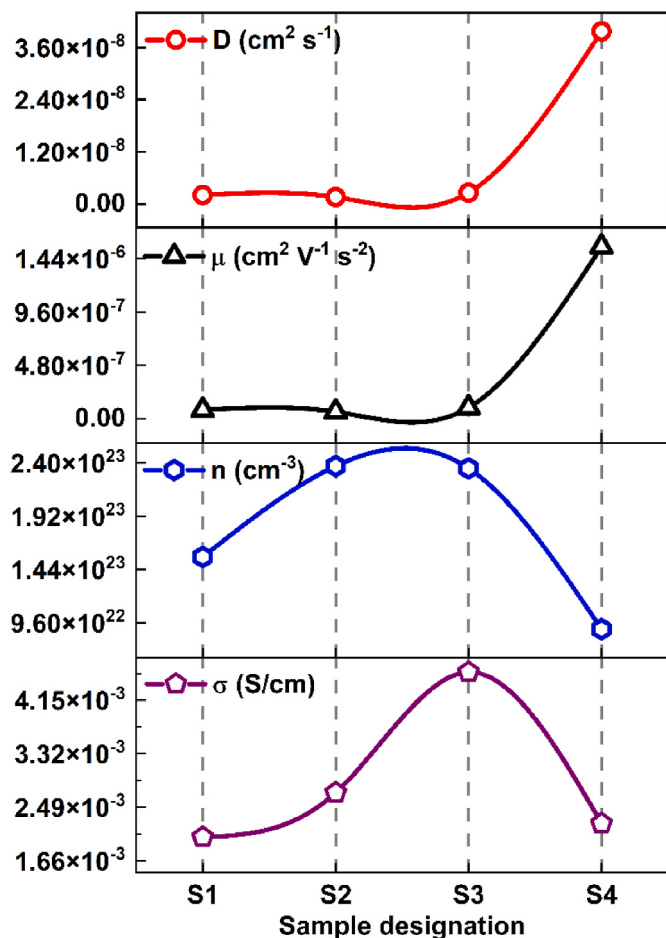


Fig. 10. Variation of transport properties for irradiated samples.

ion-blocking nature of stainless steel. The high-frequency semi-circular arc represents the bulk phenomenon-ion/electron conduction in bulk and the capacitance due to the dipoles in bulk. Considering these facts, an electrical equivalent circuit (EEC) is chosen. The ideal Nyquist plot is a perfect semicircle followed by a spike parallel to the y-axis (EEC given in Fig. 7(b)). Since the plot deviates from the ideal behaviour, the capacitor is replaced by a constant phase element (CPE). Thus, the equivalent circuit consists of a parallel combination of bulk resistance R_b and constant phase element CPE1, in series with another constant phase element CPE2. The intercept of the semi-circular arc can evaluate the bulk resistance to the flow of ions/electrons with Z_r axis. It can also be found by fitting the Nyquist plot with the above EEC (black circles are experimental values, and fitting is a solid red line in Fig. 7(a)). The bulk resistance from the intercept method matches that obtained using the EEC method. Using R_b one can calculate the bulk conductivity (σ) using the expression $= \frac{t}{R_b A}$, where t is the thickness, and A is the effective contact area.

The value of bulk conductivity for the unirradiated sample measured at room temperature stood at 1.40×10^{-4} S/cm, aligning with our previous findings. Upon irradiation, the bulk resistance drops and becomes minimum for the S3 sample, and an increment was observed at higher fluence (S4), thus reducing the conductivity. The variation in the bulk resistance can be attributed to enhancement in the amorphous phase of the polymer matrix along with the dissociation of NaBr salt in the polymer matrix, as confirmed by dielectric studies. A similar observation has been reported by Hanafy (2008), where the increase in the conductivity is due to the formation of energetic free electrons, free ions, and free radicals. This suggests that neutron irradiation can further enhance the bulk conductivity of polymer electrolytes. Among all

irradiated samples, Sample S3 has the highest ionic conductivity, displaying an order increase compared to the unirradiated sample.

3.7. AC conductivity studies

The conductivity as a function of frequency is studied by plotting the real part of complex conductivity, as shown in Fig. 8. The plot clearly shows two distinct regions. (i) Low-frequency dispersion region where the conductivity is low due to the electrode polarization effect. (ii) Mid-frequency region where the ac conductivity is independent of frequency represented by a flat region. Extrapolating this flat region onto σ_{ac} axis at $\omega = 0$ gives the dc conductivity. The values have been tabulated in Table 5. Usually, the ac spectra consist of a third region (iii) high-frequency dispersion region where ac conductivity follows a power law $\sigma_{ac} \approx \omega^s$. However, this region cannot be observed in Fig. 8 as it does not appear within the measurement frequency range. Due to the absence of region (iii), the Jonscher power law cannot be used to fit the ac spectra since this law is only applicable for region (ii) and region (iii). Upon irradiation, the plot gets shifted to a higher conductivity side. The dc conductivity obtained via the intercept method agrees well with the bulk conductivity from the Nyquist plot's.

3.8. Dielectric studies

The dynamics of the polymeric system are reflected by the dielectric response expressed in terms of the complex dielectric permittivity over a frequency range of 100 Hz to 5 MHz. This response captures all contributions to the frequency-dependent polarization. It consists of an in-phase real component ϵ' representing the ability to store energy and an out-of-phase imaginary component ϵ'' representing the energy loss due to fluctuating molecular dipoles and the charge carrier motion. Fig. 9(a) and (b) show the variation of ϵ' and ϵ'' as a function of frequency. The dispersion of ϵ' and ϵ'' at lower frequencies is due to the electrode polarization (EP) effect (Utpalla et al., 2021). Due to the ion-blocking nature of the stainless-steel electrode used for the measurement, ions accumulate at the opposite electrodes forming the double layer, whereas the electrons pass through the outer circuit. Double-layer formation is responsible for the high dielectric constant at low frequencies. Since carriers are no longer able to follow the field at higher frequencies, there is a monotonic decrease in ϵ' and ϵ'' . The value of ϵ' increased with the fluence and became maximum for the S3 sample, while S4 exhibited decreased ϵ' compared to S3 (refer to Table 6). This is attributed to an increase in free ions in the polymer bulk, as indicated by the expression $n = n_0 \exp\left(-\frac{U}{k_b T}\right)$ where symbols have usual meaning (Cyriac et al., 2022c). The increase in the free ion concentration is mainly due to the further dissociation of NaBr salt in the matrix (Abdul Rahaman et al., 2014) and also due to the formation of free ions due to irradiation (Hanafy, 2008). Thus, S3 has the highest free ion concentration among all the samples corroborating the transport property study. The decrement in the carrier concentration for the S4 sample may be due to the crosslinking process and/or formation of contact ions or larger ion aggregates at higher fluence. This can be easily proved by the FTIR deconvolution method if the salt ions are IR active. In the current study, this method is not possible since Na^+ or Br^- ions are IR inactive.

Fig. 9(c) shows the variation of the tangent loss for all the polymer samples. The plot shows a characteristic maximum indicating the conduction relaxation in the samples. This peak is found to shift to a higher frequency with an increased influence up to the S3 sample, then slightly shifts back for the S4 sample. This rightward shift indicates the lowering of relaxation time, indicating the faster ion dynamics due to the decrement in the crystallinity of the samples (Koduru et al., 2017).

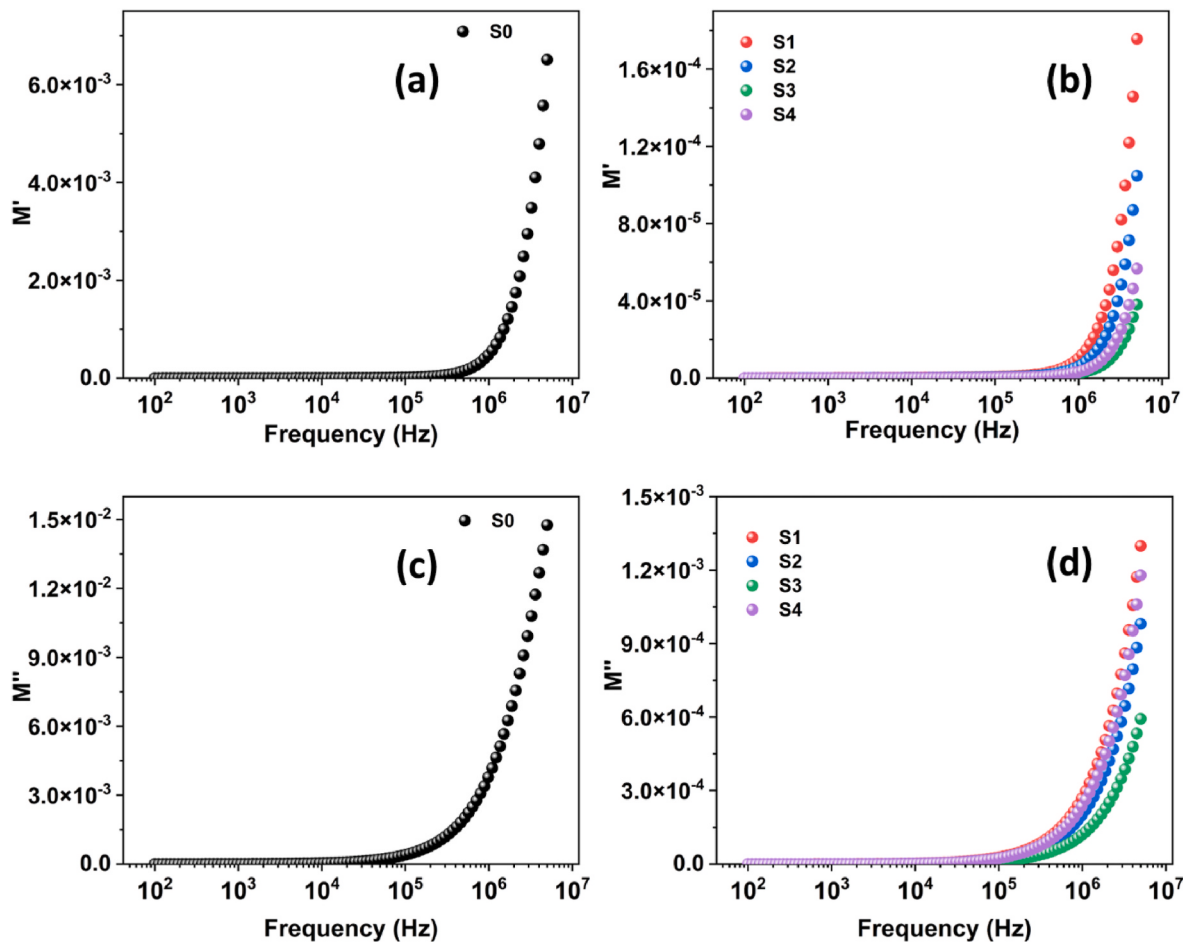


Fig. 11. Plot of (a) real part of modulus for S0 (b) real part of modulus for S1–S4 (c) imaginary part of modulus for S0 (d) imaginary part of modulus for S1–S4.

3.9. Transport properties study

Identifying the variation of the transport variables such as carrier concentration (n), diffusion coefficient (D), and mobility (μ) will help to understand the parameter which influences the bulk conductivity. There are several methods to study the transport property, such as Nyquist plot fitting, FTIR Deconvolution method, Trukhan model, B-M Method etc. We have used the Nyquist plot fitting proposed by Arof and co-workers (Arof et al., 2014). According to this method, the Nyquist plots, which show depressed semicircle and a slanted spike are fitted using the following equations.

$$Z_r = \frac{R + R^2 k_1^{-1} \omega^{p_1} \cos\left(\frac{\pi p_1}{2}\right)}{1 + 2Rk_1^{-1} \omega^{p_1} \cos\left(\frac{\pi p_1}{2}\right) + R^2 k_1^{-2} \omega^{2p_1}} + \frac{\cos\left(\frac{\pi p_2}{2}\right)}{k_2^{-1} \omega^{p_2}} \quad (4)$$

$$Z_i = \frac{R^2 k_1^{-1} \omega^{p_1} \sin\left(\frac{\pi p_1}{2}\right)}{1 + 2Rk_1^{-1} \omega^{p_1} \cos\left(\frac{\pi p_1}{2}\right) + R^2 k_1^{-2} \omega^{2p_1}} + \frac{\sin\left(\frac{\pi p_2}{2}\right)}{k_2^{-1} \omega^{p_2}} \quad (5)$$

The parameters R , k_1^{-1} , k_2^{-1} , p_1 , p_2 have usual meaning and has been defined in the article by Arof et al. using the fitted parameters in equations (4) and (5), the transport variables of charge carriers are estimated with the following equations.

$$D = \frac{e(k_2 \epsilon_r \epsilon_0 A)^2}{\tau_2} \quad (6)$$

$$\mu = \frac{eD}{k_B T} \quad (7)$$

$$n = \frac{\sigma}{\mu e} \quad (8)$$

Here ϵ_r , k_B , T and τ_2 have the usual meaning. The variation of these parameters for irradiated samples has been listed in Table 6

To have a better idea, the variation of these parameters has been represented in Fig. 10.

As discussed in dielectric studies, the dielectric constant ϵ' at low frequency indicates the free ion concentration. The carrier concentration variation, dielectric constant, and conductivity follow the same trend. Since ionic conductivity is related to carrier concentration by $\sigma = ne\mu$ (Awadhia and Agrawal, 2007), the increment in the carrier concentration strongly influences the conductivity with neutron irradiation.

3.10. Modulus spectra studies

The electric modulus M^* is defined as the reciprocal of complex permittivity ϵ^* as

$$M^* = \frac{1}{\epsilon^*} = M' + jM'' = \frac{\epsilon'}{\epsilon'^2 + \epsilon''^2} + j \frac{\epsilon''}{\epsilon'^2 + \epsilon''^2}$$

This representation is advantageous over dielectric formalism as it suppresses the electrode polarization (EP), which masks the relaxation process in dielectric formalism. Also, the type of electrode, electrode-electrolyte contact, and any adsorbed impurities do not affect the modulus spectra (Utpalla et al., 2021). The plot of M' usually shows conductivity relaxation peaks. Fig. 11 shows the variation of M' and M'' as a function of frequency for the polymer samples at room temperature. Both M' and M'' at low frequency has negligible values with long tails,

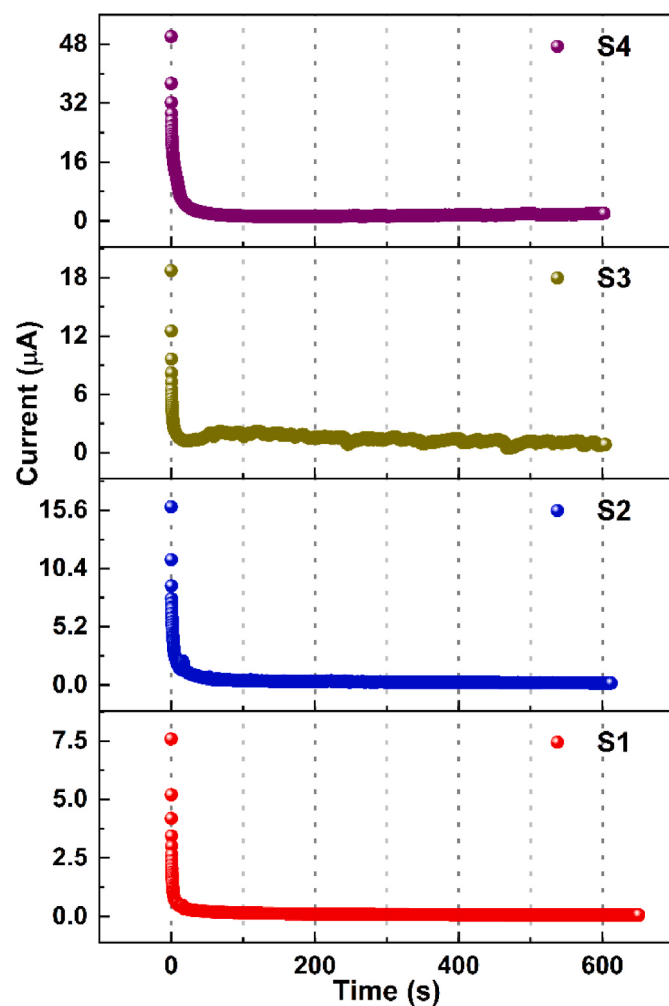


Fig. 12. Current versus time plots for irradiated samples.

Table 7

Variation of ionic and electronic transference number, ionic and electronic conductivity for irradiated samples.

Sample	t_{ion}	t_e	σ_i (S/cm)	σ_e (S/cm)
S1	0.992	0.008	2.01×10^{-3}	1.62×10^{-5}
S2	0.990	0.010	2.69×10^{-3}	2.71×10^{-5}
S3	0.955	0.045	4.38×10^{-3}	2.06×10^{-4}
S4	0.960	0.040	2.15×10^{-3}	8.95×10^{-5}

indicating the large capacitance due to EP (Ravi et al., 2011). It is found that the M' shows a dispersion behaviour at high frequencies but does not saturate to M_∞ at high frequencies. This dispersion behaviour is due to the spread of conductivity relaxation over a wide frequency range indicating presence of relaxation time. This is usually accompanied by a relaxation peak in the M' plot. The absence of peak in the M' plot is due to the fact that M is equivalent to e (Aziz et al., 2010). In the given frequency range, well-defined peaks were not observed in M' plot. Nevertheless, with the increasing fluence, the high-frequency dispersion region shifted to the right mainly due to the bulk effect indicating the increase in the flexibility of the polymer matrix (Hema et al., 2008) (see Fig. 11).

3.11. Transference number measurement (TNM) studies

TNM was done to identify the major charge carriers. The polymer electrolyte to be used in the energy storage devices must have ions as

majority charge carriers. Under the Wagner polarization technique, the symmetric cell consisting of polymer electrolyte sandwiched between stainless steel electrodes was polarized for a long time using a dc potential of 0.5 V and monitoring current as a function of time (Fig. 12). Initial high current (I_i) is due to ions as they are blocked by electrodes and a final minor current (I_f) arises from electrons. The following equations are used to calculate ionic transference (t_{ion}) number and hence electron transference number (t_{elec})

$$t_{ion} = 1 - \frac{I_f}{I_i}$$

$$t_{elec} = 1 - t_{ion}$$

Using the bulk conductivity and transference number, ionic and electronic conductivity (σ_i, σ_e) can be calculated using the following equations

$$\sigma_i = \sigma_{bulk} \times t_{ion}$$

$$\sigma_e = \sigma_{bulk} \times t_{elec}$$

The values of transference number, ionic and electronic conductivity are tabulated in Table 7.

The high value of the ionic transference number close to 1 indicates that ions are major charge carriers. In addition, the prepared polymer electrolytes exhibit high ionic current and low electron current, which is another criterion for an efficient polymer electrolyte. Our previous work reported the total ionic transference number for the pristine sample to be 0.99. A decrement in ionic transference number for irradiated samples compared to pristine sample indicates the formation of free radicals (electrons) due to the irradiation process leading to a higher number of electrons.

4. Conclusion

This study delves into the preparation of Ag incorporated PVA-NaBr solid polymer electrolytes via a simple solution casting technique. The impact of fast neutron radiation on various aspects—optical, structural, morphological, thermal, and electrical conductivity—was systematically investigated. The XRD analysis confirmed the decline in crystallinity at lower fluence, followed by the increase at higher fluence, clearly indicating the structural modifications post-irradiation. FTIR studies revealed significant change in transmittance and wavenumber position, indicating simultaneous bond formation and breakage, resulting in structural changes. Notably, the FTIR results highlighted that at a lower fluence, cross-linking dominated, while higher fluence induced more chain scissions compared to cross linking. UV-Visible analysis showcased increased absorbance below 300 nm, along with a shift in the SPR peak at lower and higher fluence levels, indicating modifications in the material's optical properties. Moreover, there was a decrease in the bandgap and an elevation in Urbach energy post-irradiation, aligning well with the FTIR observations. Morphological changes were evident in FESEM images following exposure to fast neutrons, while TGA curves demonstrated enhanced thermal stability after irradiation. Transport properties, analyzed via Nyquist plot fitting, elucidated variations in carrier concentration, mobility, and diffusion coefficient fluctuation. Remarkably, the maximum room temperature conductivity increased significantly with neutron fluence, reaching 4.38×10^{-3} S/cm, substantially higher than the unirradiated sample. Transference number measurements (TNM) highlighted ions as the predominant charge carriers rather than electrons. Hence the current study demonstrated that fast neutron irradiation is one of the feasible and potential approaches for tuning the conductivity of polymer electrolytes and the possibility of using neutron irradiated Ag incorporated PVA- NaBr solid polymer electrolyte for energy storage applications.

CRediT authorship contribution statement

M.P. Shilpa: Conceptualization, Data curation, Formal analysis, Investigation, Methodology, Visualization, Writing – original draft, Writing – review & editing. **Vipin Cyriac:** Conceptualization, Data curation, Formal analysis, Investigation, Methodology, Writing – original draft, Writing – review & editing. **S.C. Gurumurthy:** Conceptualization, Investigation, Methodology, Project administration, Supervision, Validation, Writing – review & editing. **Ismayil:** Conceptualization, Investigation, Methodology, Supervision, Writing – review & editing. **Sachin Shet:** Conceptualization, Investigation, Methodology, Writing – review & editing. **K.V. Subbaiah:** Conceptualization, Investigation, Methodology, Writing – review & editing. **M.S. Murari:** Investigation, Methodology, Writing – review & editing.

Declaration of competing interest

The authors declare that they have no known competing financial interests or personal relationships that could have appeared to influence the work reported in this paper.

Data availability

Data will be made available on request.

Acknowledgements

Shilpa M P, Vipin Cyriac, Gurumurthy S C, and Ismayil acknowledge Manipal Academy of Higher Education for the funding facility. One of the authors, Vipin Cyriac, acknowledges the financial assistance from the "Directorate of Minorities, Bengaluru, Government of Karnataka" in the form of "Directorate of Minorities Fellowship for Minority Students," sanction order: DOM/Fellowship/CR-10/2019-20 dated June 29, 2020. The authors also thank Dr Ganesh Sanjeev and Shreedatta Hegde, Department of studies in Physics, Mangalore University, for providing the facility for impedance spectroscopy studies.

References

- Abd El-Kader, F.H., Gaafar, S.A., Rizk, M.S., Kamel, N.A., 1999. Optical studies of pure and gelatin-doped poly(vinyl alcohol) films irradiated with fast neutrons. *J. Appl. Polym. Sci.* 72, 1395–1406. [https://doi.org/10.1002/\(SICI\)1097-4628\(19990613\)72:11<1395::AID-APP3>3.0.CO;2-8](https://doi.org/10.1002/(SICI)1097-4628(19990613)72:11<1395::AID-APP3>3.0.CO;2-8).
- Abd El-Kader, F.H., Osman, W.H., Ragab, H.S., Shehab, A.M., Rizk, M.S., Basha, M.A.F., 2004. Electrical and optical properties of polyvinyl alcohol thin films doped with metal salts. *J. Polym. Mater.* 21, 49–60.
- Abdel-Zaher, N.A., Moselhey, M.T.H., Guirguis, O.W., 2016. Effect of fast neutrons on the structure and thermal properties of PVA/HPMC blends. *Journal of Thermal Analysis and Calorimetry* 126, 1289–1299. <https://doi.org/10.1007/S10973-016-5675-4/TABLES/3>.
- Abdul Rahaman, M.H., Khandaker, M.U., Khan, Z.R., Kufian, M.Z., Noor, I.S.M., Arof, A. K., 2014. Effect of gamma irradiation on poly(vinylidene difluoride)-lithium bis (oxalato)borate electrolyte. *Phys. Chem. Chem. Phys.* 16, 11527–11537. <https://doi.org/10.1039/C4CP01233J>.
- Abuali Galehdari, N., Kelkar, A.D., 2017. Effect of neutron radiation on the mechanical and thermophysical properties of nanoengineered polymer composites. *J. Mater. Res.* 32, 426–434. <https://doi.org/10.1557/jmr.2016.494>.
- Abutalib, M.M., Guirguis, O.W., 2014. Influence of fast neutron irradiation on the optical properties of poly (vinyl alcohol)/hydroxypropyl cellulose blends. *Br. J. Appl. Sci. Technol.* 4, 4316. <https://doi.org/10.9734/BJAST/2014/12723>.
- Abutalib, M.M., Abdel-Zaher, N.A., Xiao, R., 2015. Study of the thermal and structural properties of PVA/HPC blends due to fast neutrons irradiation. *Current Journal of Applied Science and Technology* 11, 1–12. <https://doi.org/10.9734/BJAST/2015/20495>.
- Ali, Z.I., Saleh, H.H., Afify, T.A., 2014. Optical, structural and catalytic evaluation of gamma-irradiation synthesized Ag/PVA nanocomposite films. *Int. J. Eng. Res. Technol.* 3, 1527–1538.
- Althubiti, N.A., Abdelhamied, M.M., Abdelreheem, A.M., Atta, A., 2022. Oxygen irradiation induced modification on the linear and nonlinear optical behavior of flexible MC/PANI/Ag polymeric nanocomposite films. *Inorg. Chem. Commun.* 137, 109229 <https://doi.org/10.1016/j.inoche.2022.109229>.
- Althubiti, N.A., Atta, A., Alotaibi, B.M., Abdelhamied, M.M., 2023a. Structural and dielectric properties of ion beam irradiated polymer/silver composite films. *Surf. Innovations* 11, 90–100. <https://doi.org/10.1680/jsuin.22.00010>.
- Althubiti, N.A., Atta, A., Abdeltwab, E., Al-Harbi, N., Abdel-Hamid, M.M., 2023b. Structural characterization and dielectric properties of low energy hydrogen beam irradiated PVA/ZnO nanocomposite materials. *Inorg. Chem. Commun.* 153, 110779 <https://doi.org/10.1016/j.inoche.2023.110779>.
- Arof, A.K., Amirudin, S., Yusof, S.Z., Noor, I.M., 2014. A method based on impedance spectroscopy to determine transport properties of polymer electrolytes. *Phys. Chem. Chem. Phys.* 16, 1856–1867.
- Arya, A., Sharma, A.L., 2017. Polymer electrolytes for lithium ion batteries: a critical study. *Ionics* 23 (3), 497–540. <https://doi.org/10.1007/S11581-016-1908-6>, 23 (2017).
- Atta, A., Abdeltwab, E., 2021. Influence of ion irradiation on the surface properties of silver-coated flexible PDMS polymeric films. *Braz. J. Phys.* 52, 3. <https://doi.org/10.1007/s13538-021-01011-5>.
- Atta, A., Alotaibi, B.M., Abdelhamied, M.M., 2022. Structural characteristics and optical properties of methylcellulose/polyaniline films modified by low energy oxygen irradiation. *Inorg. Chem. Commun.* 141, 109502 <https://doi.org/10.1016/j.inoche.2022.109502>.
- Awadhia, A., Agrawal, S.L., 2007. Structural, thermal and electrical characterizations of PVA:DMSO:NH4SCN gel electrolytes. *Solid State Ionics* 178, 951–958. <https://doi.org/10.1016/J.JSSI.2007.04.001>.
- Aziz, S.B., Abidin, Z.H.Z., Arof, A.K., 2010. Influence of silver ion reduction on electrical modulus parameters of solid polymer electrolyte based on chitosan-silver triflate electrolyte membrane. *Express Polym. Lett.* 4, 300–310. <https://doi.org/10.3144/expresspolymlett.2010.38>.
- Bafandeh, N., Larijani, M.M., Shafeikhani, A., Hantehzadeh, M.R., Sheikh, N., 2016. Synthesis of polyaniline films: case study on post gamma irradiation dose. *J. Mater. Sci. Mater. Electron.* 27 (10), 10566–10572. <https://doi.org/10.1007/S10854-016-5151-8>, 27 (2016).
- Basha, A.F., Basha, M.A.F., 2017. Impact of neutron irradiation on the structural and optical properties of PVP/gelatin blends doped with dysprosium (III) chloride. *J. Appl. Phys.* 122, 235104 <https://doi.org/10.1063/1.5008494>.
- Bhat, N.V., Nate, M.M., Kurup, M.B., Bambole, V.A., Sabharwal, S., 2005. Effect of γ -radiation on the structure and morphology of polyvinyl alcohol films. *Nuclear Instruments and Methods in Physics Research Section B: Beam Interactions with Materials and Atoms* 237, 585–592. <https://doi.org/10.1016/J.NIMB.2005.04.058>.
- Briskman, B.A., 2007. Specificity of proton irradiation effects on polymers. *Nuclear Instruments and Methods in Physics Research Section B: Beam Interactions with Materials and Atoms* 265, 72–75. <https://doi.org/10.1016/j.nimb.2007.08.028>.
- Chahal, R.P., Mahendia, S., Tomar, A.K., Kumar, S., 2012. γ -Irradiated PVA/Ag nanocomposite films: materials for optical applications. *J. Alloys Compd.* 538, 212–219. <https://doi.org/10.1016/J.JALLCOM.2012.05.085>.
- Chikaoui, K., Izzerouken, M., Djebara, M., Abdesselam, M., 2017. Polyethylene terephthalate degradation under reactor neutron irradiation. *Radiat. Phys. Chem.* 130, 431–435. <https://doi.org/10.1016/J.RADPHYSCHM.2016.10.002>.
- Croonenborghs, B., Smith, M.A., Strain, P., 2007. X-ray versus gamma irradiation effects on polymers. *Radiat. Phys. Chem.* 76, 1676–1678. <https://doi.org/10.1016/J.radiophyschem.2007.01.014>.
- Cyriac, V., Molakalu Padre, S., Ismayil, Sangam Chandrashekhar, G., Chavan, C., Fakereappa Bhajantri, R., Murari, M.S., 2022a. Tuning the ionic conductivity of flexible polyvinyl alcohol/sodium bromide polymer electrolyte films by incorporating silver nanoparticles for energy storage device applications. *J. Appl. Polym. Sci.* 139, e52525 <https://doi.org/10.1002/APP.52525>.
- Cyriac, V., Ismayil, Noor, I.M., Mishra, K., Chavan, C., Bhajantri, R.F., Masti, S.P., 2022b. Ionic conductivity enhancement of PVA: carboxymethyl cellulose poly-blend electrolyte films through the doping of NaI salt. *Cellulose* 29, 3271–3291. <https://doi.org/10.1007/s10570-022-04483-z>.
- Cyriac, V., Ismayil, Noor, I.S.B.M., Rojidi, Z.E., Sudhakar, Y.N., Chavan, C., Bhajantri, R.F., Murari, M.S., 2022c. Modification in the microstructure of sodium carboxymethylcellulose/polyvinyl alcohol polyblend films through the incorporation of NaNO₃ for energy storage applications. *Int. J. Energy Res.* 46, 22845–22866. <https://doi.org/10.1002/er.8588>.
- Eisa, W.H., Abdel-Moneam, Y.K., Shaaban, Y., Abdel-Fattah, A.A., Abou Zeid, A.M., 2011. Gamma-irradiation assisted seeded growth of Ag nanoparticles within PVA matrix. *Mater. Chem. Phys.* 128, 109–113. <https://doi.org/10.1016/J.MATCHEMPHYS.2011.02.076>.
- El-Malawy, D., Hassan, H.E., El Ghazaly, M., Abdel Samad, S., Al-Abyad, M., 2023. Low-energy α -particle irradiation of polymeric-based nanofiller. *Eur. Phys. J. Plus* 138, 759. <https://doi.org/10.1140/epjp/s13360-023-04300-x>.
- El-Sawy, N.M., El-Arnaouty, M.B., Abdel Ghaffar, A.M., 2010. γ -Irradiation Effect on the Non-cross-linked and Cross-Linked Polyvinyl Alcohol Films, vol. 49, pp. 169–177. <https://doi.org/10.1080/03602550903284248>.
- El-Zahhar, A.A., Yassien, K.M., El-Bakary, M.A., 2020. Study on the thermal and structural properties of gamma-irradiated polyethylene terephthalate fibers. *J. Polym. Eng.* 40, 129–135. <https://doi.org/10.1515/POLYENG-2019-0234/MACHINEREADABLELICITATION/RIS>.
- Ferreño, D., Mañanes, A., Rábago, D., Casado, J.A., González, J.A., Gómez, S., Carrascal, I.A., Ruiz, E., Diego, S., Gómez, F., Sarachaga, E., 2018. Mechanical behavior and microstructural changes in polyurethane exposed to high doses of X rays, gamma rays or neutron irradiation. *Polym. Test.* 67, 359–369. <https://doi.org/10.1016/j.polymertesting.2018.03.033>.
- Ghosal, S., Ray, R., Ballabh, T.K., Tarafdar, S., 2013. Study of diffusion and conduction in gamma irradiated solid polymer electrolytes by fractal model structure. *Indian J. Pure Appl. Phys.* 51, 324–327. <https://doi.org/10.1007/s00289-007-0850-1>.
- Gomaa, M.M., Hugenschmidt, C., Dickmann, M., Abdel-Hady, E.E., Mohamed, H.F.M.M., Abdel-Hamed, M.O., 2018. Crosslinked PVA/SSA proton exchange membranes: correlation between physicochemical properties and free volume determined by

- positron annihilation spectroscopy. *Phys. Chem. Chem. Phys.* 20, 28287–28299. <https://doi.org/10.1039/C8CP05301D>.
- Gongxu, L., Hongying, C., Dongyuan, L., 1993. The degradation in solid state of polyvinyl alcohol by gamma-irradiation. *Radiat. Phys. Chem.* 42, 229–232. [https://doi.org/10.1016/0969-806X\(93\)90240-U](https://doi.org/10.1016/0969-806X(93)90240-U).
- Guirguis, O.W., Moseley, M.T.H., 2011. Optical study of poly(vinyl alcohol)/hydroxypropyl methylcellulose blends. *J. Mater. Sci.* 46, 5775–5789. <https://doi.org/10.1007/S10853-011-5533-5/TABLES/7>.
- Hanafy, T.A., 2008. Drastic effects of fast neutrons and γ -irradiation on the DC conductivity of Co-, Ni-, Mn- and Ag-gelatin doped films. *Curr. Appl. Phys.* 8, 527–534. <https://doi.org/10.1016/J.CAP.2007.09.002>.
- Hema, M., Selvasekerapandian, S., Sakunthala, A., Arunkumar, D., Nithya, H., 2008. Structural, vibrational and electrical characterization of PVA–NH4Br polymer electrolyte system. *Phys. B Condens. Matter* 403, 2740–2747. <https://doi.org/10.1016/J.PHYSB.2008.02.001>.
- Hodge, R.M., Edward, G.H., Simon, G.P., 1996. Water absorption and states of water in semicrystalline poly(vinyl alcohol) films. *Polymer* 37, 1371–1376. [https://doi.org/10.1016/0032-3861\(96\)81134-7](https://doi.org/10.1016/0032-3861(96)81134-7).
- Htwe, Y.Z.N., Mariatti, M., 2020. Fabrication and characterization of silver nanoparticles/PVA composites for flexible electronic application. *AIP Conf. Proc.* 2267, 020046. <https://doi.org/10.1063/5.0016135>.
- Koduru, H.K., Marino, L., Scarpelli, F., Petrov, A.G., Marinov, Y.G., Hadjichristov, G.B., Iliev, M.T., Scaramuzza, N., 2017. Structural and dielectric properties of NaIO4 – complexed PEO/PVP blended solid polymer electrolytes. *Curr. Appl. Phys.* 17, 1517–1531. <https://doi.org/10.1016/J.CAP.2017.07.012>.
- Kumar, V., Sonkawade, R.G., Chakarvarti, S.K., Kulriya, P., Kant, K., Singh, N.L., Dhaliwal, A.S., 2011. Study of optical, structural and chemical properties of neutron irradiated PADC film. *Vacuum* 86, 275–279. <https://doi.org/10.1016/J.VACUUM.2011.07.001>.
- Kumar, V., Sonkawade, R.G., Chakarvarti, S.K., Singh, P., Dhaliwal, A.S., 2012. Carbon ion beam induced modifications of optical, structural and chemical properties in PADC and PET polymers. *Radiat. Phys. Chem.* 81, 652–658. <https://doi.org/10.1016/J.RADPHYSCHM.2012.02.027>.
- Long, L., Wang, S., Xiao, M., Meng, Y., 2016. Polymer electrolytes for lithium polymer batteries. *J. Mater. Chem. A* 4, 10038–10069. <https://doi.org/10.1039/C6TA02621D>.
- Mathakaria, N.L., Bhoraskar, V.N., Dhole, S.D., 2014. A Comparative Study on the Effects of Co-60 Gamma Radiation on Polypropylene and Polyimide, vol. 169, pp. 779–790. <https://doi.org/10.1080/10420150.2014.939176>, 10.1080/10420150.2014.939176.
- Nafee, S.S., Hamdalla, T.A., 2019. Effect of neutron irradiation on the optical properties of PMMA/RhB used in optical fiber amplification. *J. Radioanal. Nucl. Chem.* 320 (1), 101–108. <https://doi.org/10.1007/S10967-019-06440-W>, 320 (2019).
- Naghavi, K., Saion, E., Rezaee, K., Yunus, W.M.M., 2010. Influence of dose on particle size of colloidal silver nanoparticles synthesized by gamma radiation. *Radiat. Phys. Chem.* 79, 1203–1208. <https://doi.org/10.1016/J.RADPHYSCHM.2010.07.009>.
- Naikwadi, A.T., Sharma, B.K., Bhatt, K.D., Mahanwar, P.A., 2022. Gamma radiation processed polymeric materials for high performance applications: a review. *Front. Chem.* 10. <https://www.frontiersin.org/articles/10.3389/fchem.2022.837111>. (Accessed 27 December 2023).
- Nanda, P., Maity, S., Pandey, N., Ray, R., Thakur, A.K., Tarafdar, S., 2011. Conductivity enhancement in polymer electrolytes on gamma irradiation. *Radiat. Phys. Chem.* 80, 22–27. <https://doi.org/10.1016/J.RADPHYSCHM.2010.09.003>.
- Nasef, M.M., Dahlan, K.Z.M., 2003. Electron irradiation effects on partially fluorinated polymer films: structure–property relationships. *Nuclear Instruments and Methods in Physics Research Section B: Beam Interactions with Materials and Atoms* 201, 604–614. [https://doi.org/10.1016/S0168-583X\(02\)02068-2](https://doi.org/10.1016/S0168-583X(02)02068-2).
- Ngai, K.S., Ramesh, S., Ramesh, K., Juan, J.C., 2016. A review of polymer electrolytes: fundamental, approaches and applications. *Ionics* 22, 1259–1279. <https://doi.org/10.1007/s11581-016-1756-4>.
- Noor, I.S., Majid, S.R., Arof, A.K., 2013. Poly(vinyl alcohol)-LiBOB complexes for lithium-air cells. *Electrochim. Acta* 102, 149–160. <https://doi.org/10.1016/J.ELECTACTA.2013.04.010>.
- Nouh, S.A., Nabiy, A.A., El Hussieny, H.M., 2007. Fast Neutron Irradiation Effects in PM-355 Nuclear Track Detector, vol. 65, pp. 1173–1178. <https://doi.org/10.1016/J.APRAUDIO.2007.04.017>.
- Philipp, W.H., Hsu, L.C., 1979. Three Methods for in Situ Cross-Linking of Polyvinyl Alcohol Films for Application as Ion-Conducting Membranes in Potassium Hydroxide Electrolyte (No. NASA-TP-1407).
- Prasher, S., Kumar, M., 2019. Effects of neutron irradiation on polymer, 351–368. https://doi.org/10.1007/978-3-030-05770-1_11.
- Raghu, S., Archana, K., Sharannappa, C., Ganesh, S., Devendrappa, H., 2016. Electron beam and gamma ray irradiated polymer electrolyte films: dielectric properties. *Journal of Radiation Research and Applied Sciences* 9, 117–124. <https://doi.org/10.1016/j.jrras.2015.10.007>.
- Ravi, M., Pavani, Y., Kiran Kumar, K., Bhavani, S., Sharma, A.K., Narasimha Rao, V.V.R., 2011. Studies on electrical and dielectric properties of PVP:KBrO4 complexed polymer electrolyte films. *Mater. Chem. Phys.* 130, 442–448. <https://doi.org/10.1016/J.MATCHEMPHYS.2011.07.006>.
- Rivaton, A., Arnold, J., Dos Santos, M., Bussière, P.O., Taviot-Gueho, C., 2010. Effect of low doses of 14 MeV neutrons on polymers. *Radiat. Res.* 174, 658–667. <https://doi.org/10.1667/RR2215.1>.
- Saeed, M.A.M., Abdullah, O.G., 2020. Effect of structural features on ionic conductivity and dielectric response of PVA proton conductor-based solid polymer electrolytes. *J. Electron. Mater.* 50, 1–11. <https://doi.org/10.1007/s11664-020-08577-x>.
- Sagar, R.N., Ravindrachary, V., Guruswamy, B., Hegde, S., Mahanthesh, B.K., Kumari, R. P., 2018. Effect of TiO2 nanoparticles doping on structural and electrical properties of PVA: NaBr polymer electrolyte. *AIP Conf. Proc.* 1953, 030216. <https://doi.org/10.1063/1.5032551>.
- Sinha, E., Rout, S.K., 2008. Effect of neutron irradiation on the structural, mechanical, and thermal properties of jute fiber. *J. Appl. Polym. Sci.* 110, 413–423. <https://doi.org/10.1002/APP.28504>.
- Tabata, Y., Katsumura, Y., 1985. Fast neutron irradiation effects on polymers-polyethylene, ethylene propylene rubber and tetrafluoroethylene propylene copolymer. *J. Nucl. Mater.* 133–134, 781–784. [https://doi.org/10.1016/0022-3115\(85\)90256-9](https://doi.org/10.1016/0022-3115(85)90256-9).
- Torres, F.G., De-La-Torre, G.E., Gonzales, K.N., Troncoso, O.P., 2020. Bacterial-polymer-based electrolytes: recent progress and applications. *ACS Appl. Energy Mater.* 3.
- Utpalla, P., Sharma, S.K., Deshpande, S.K., Bahadur, J., Sen, D., Sahu, M., Pujari, P.K., 2021. Role of free volumes and segmental dynamics on ion conductivity of PEO/LiTFSI solid polymer electrolytes filled with SiO2 nanoparticles: a positron annihilation and broadband dielectric spectroscopy study. *Phys. Chem. Chem. Phys.* 23, 8585–8597. <https://doi.org/10.1039/D1CP00194A>.
- Wang, H., Sheng, L., Yasin, G., Wang, L., Xu, H., He, X., 2020. Reviewing the current status and development of polymer electrolytes for solid-state lithium batteries. *Energy Storage Mater.* 33, 188–215. <https://doi.org/10.1016/j.ensm.2020.08.014>.
- Williams, F., 1972. Early processes in radiation chemistry and the reactions of intermediates. *The Radiation Chemistry of Macromolecules* 7–23. <https://doi.org/10.1016/B978-0-12-219801-4.50008-2>.
- Zhu, Y.S., Wang, X.J., Hou, Y.Y., Gao, X.W., Liu, L.L., Wu, Y.P., Shimizu, M., 2013. A new single-ion polymer electrolyte based on polyvinyl alcohol for lithium ion batteries. *Electrochim. Acta* 87, 113–118. <https://doi.org/10.1016/J.ELECTACTA.2012.08.114>.